13

Quantitative Absorption and Scattering Spectra in Thick Tissues Using Broadband Diffuse Optical Spectroscopy

DOROTA JAKUBOWSKI, FREDERIC BEVILACQUA,
SEAN MERRITT, ALBERT CERUSSI,
AND BRUCE J. TROMBERG

Near-infrared spectroscopy is a well-established technique that has been applied to a variety of medical diagnostic problems. Recent examples include detecting peripheral vascular disease, compartment syndrome, and various forms of cancer (Fantini et al., 1998; Zonios et al., 1999; Benaron et al., 2000; Giannotti et al., 2000; Tromberg et al., 2000; Wariar et al., 2000; Cerussi 2001). Because near-infrared light penetrates bone, near-infrared spectroscopy is also widely used for noninvasive brain imaging to monitor cortical activation, neonatal cerebral oxygenation, and hematomas (Adcock et al., 1999; Fantini et al., 1999; Benaron et al., 2000; Springett et al., 2000). The use of model-based *photon migration* methods to separate light absorption from scattering quantitatively in multiply scattering tissues is a type of near-infrared spectroscopy broadly referred to as *diffuse optical spectroscopy* or *DOS*.

Diffuse optical spectroscopy methods can be categorized as *time independent* and *time resolved*. Time-independent, steady-state methods use a CW source. They are capable of acquiring a full wavelength-dependent spectrum of diffuse reflectance at one time, but the data cannot be resolved into their scattering and absorbing components without additional information. Research groups using this approach have ~~used~~ multiple source–detector separations to provide this additional information (Farrell et al., 1992). Short (e.g., millimeter) source–detector separations are more sensitive to scattering properties, whereas far (e.g., centimeter) source–detector separations are sensitive to both scattering and absorption. This method provides fast and accurate results for homogenous systems. However, because two overlapping but different volumes are sampled, accuracy may suffer if the system is heterogenous or layered, as is commonly the case in tissue.

Time-resolved techniques separate absorption from scattering by launching either a single light pulse (time domain) or intensity modulations (frequency domain) into the sample. Time domain techniques measure the delay and spread of a pulse sent through the medium (Patterson et al., 1989). Frequency domain techniques, such as those used in this work, use intensity-modulated light at frequencies between 50 and 1000 MHz, and measure the phase shift and amplitude of the modulated wave as it propagates through the medium (Pham et al., 2000).

Time-resolved techniques generally require sequential scanning over optical wavelengths. This is usually satisfied by a number of diode lasers or a tunable laser. Tunable lasers are capable of acquiring a full near-infrared spectrum (Cubeddu et al., 2000). They

are finely tuned and require greater maintenance than laser diodes, posing some difficulties in a clinical setting. In contrast, diode lasers are robust but operate only at discrete wavelengths. Most such frequency domain systems measure optical properties using two to three sources (Franceschini et al., 1997; Moesta et al., 1998); a few operate with up to 7 to 10 sources. In principle, this is well above the four wavelengths necessary to quantify the four major near-infrared chromophores in tissue: deoxygenated hemoglobin, oxygenated hemoglobin, lipid, and water. Nevertheless, our recent experience suggests there is significant inaccuracy in calculating chromophore concentrations even with seven wavelengths (Bevilacqua et al., 2000).

The combined use of both steady-state and frequency domain photon migration (FDPM) techniques can provide complete absorption and scattering spectra with a single source–detector separation. This broadband DOS method expands the optical bandwidth of discrete wavelength FDPM to encompass the entire wavelength spectrum between $\approx$600 and 1000 nm. The steady-state–FDPM combination reduces dependence on the availability of specific diode wavelengths while simultaneously making the system more robust under clinical conditions. Last, it has the potential to characterize absorption backgrounds caused by minor chromophores in such tissues as muscle and brain.

The feasibility of broadband DOS has previously been shown (Bevilacqua et al., 2000). This section validates broadband DOS over a broad range of absorption and scattering values, and compares it with FDPM methods used alone. A series of water-based phantoms with known scattering and absorption properties are measured using broadband DOS and FDPM, and the derived dye concentrations are compared with those expected. As a second step, the limits of both systems are tested on a series of multiple-dye phantoms with absorption properties sufficiently high to challenge the FDPM system. We test the ability of both broadband DOS and FDPM to recover the correct absorption spectrum.

In subsequent sections we describe the application of broadband DOS to measurements of human muscle and breast tissue. These noninvasive in vivo studies highlight the sensitivity of DOS to physiological changes, particularly alterations in water and lipid content that would otherwise be impossible to recover with a standard two- to four-wavelength near-infrared spectroscopy instrument.

THEORY

Broadband DOS combines steady-state and frequency domain photon migration technologies. Combining the two systems is accomplished by joining the theoretical framework on which each is based, as illustrated in figure 13.1. The final result is a full scattering and absorption spectrum at all wavelengths from a single source–detector pair. Here we present a brief overview of this approach. For a thorough discussion and full definitions of reflectance, refer to Bevilacqua et al. (2000).

Optical properties of tissue are typically characterized by μ_a and μ_s', the absorption and reduced scattering coefficients, respectively. These parameters describe the inverse mean free paths for absorption and reduced scattering events. Reduced scattering is thus named because it attempts to take into account two independent factors: the probability of a scattering event and the angular distribution of such a scattering event. Both are functions of the optical wavelength λ. For an extensive discussion, refer to one of many sources on diffusion theory (Ishimaru, 1978; Farrell et al., 1992; Fishkin, 1994; Haskell et al., 1994).

Frequency domain photon migration methods are capable of measuring μ_a and μ_s' at discrete wavelengths. This is accomplished by recording phase lag and amplitude modulation depth as a function of modulation frequency for each laser diode used. The raw phase and amplitude are calibrated to distinguish the tissue signal from the instrument response

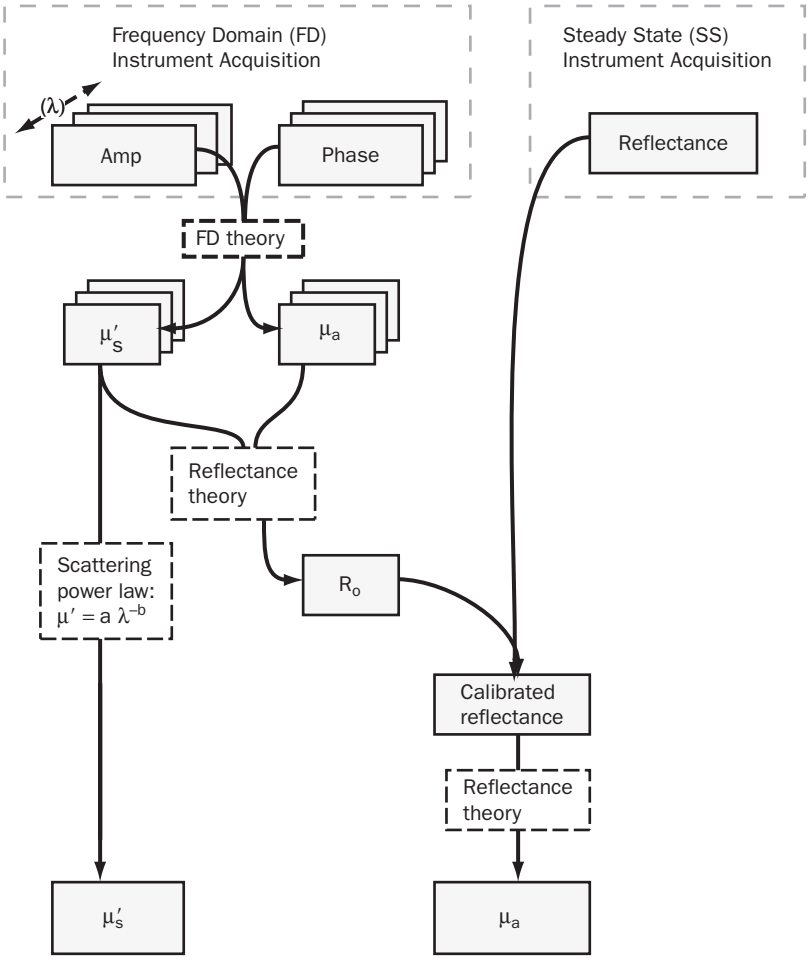

Figure 13.1 The broadband DOS algorithm. It is used for combining the raw data of the FDPM and steady-state systems. In the end, we arrive at continuous μ_a and μ_s' spectra.

using silicon phantoms of known optical properties (Pham et al., 2000). After the amplitude and phase data for a given wavelength are calibrated, it is fit using the P1 diffusion approximation under appropriate semi-infinite boundary conditions, as detailed by Fishkin (1994). The phase and amplitude data are fit simultaneously. Conversely, the real or imaginary components can be fit instead of the original phase and amplitude. Thus, we obtain the free parameters of the fit—in other words, the optical properties $\mu_a(\lambda)$ and $\mu_s'(\lambda)$—of the sample at that wavelength, λ.

In contrast, steady-state methods provide relative diffuse reflectance data for multiple wavelengths over a broad (e.g., ≈600–1000 nm) spectral region. Although μ_a and μ_s' cannot be determined from the steady-state spectra, specific pairs can be evaluated for discrete diode wavelengths. To combine steady state with FDPM, the distribution of scatterers in tissue is described by a power law:

$$\mu_s'(\lambda) = a\lambda^{-b}$$

This equation is an approximation based on Mie theory with a wide distribution of scatterers (Graaff et al., 1992; Mourant et al., 1997). It is additionally supported by numerous studies in tissue (Graaff et al., 1992; Mourant et al., 1997, 1998). By applying this equation to the

6 to 10 FDPM-derived μ_s' values, the a and b parameters, and therefore the full μ_s' spectrum, can be determined for our region of interest.

Last, we must consider that the steady-state reflectance measurement is relative. It varies by a constant R_o from the absolute reflectance R. However, the FDPM-derived μ_a and μ_s' pair can be used to calculate the true absolute reflectance R (a function of μ_a and μ_s' at any given wavelength) at 6 to 10 wavelengths. Comparing the measured with the calculated reflectance gives us R_o. With R and μ_s' determined for all wavelengths, μ_a can be calculated at each wavelength. We thus arrive at the full μ_a spectrum for all wavelengths in the 600- to 1000-nm region.

To arrive at chromophore concentrations, the μ_a spectrum is fit using the Beer-Lambert law. For a given chromophore, the μ_a contribution as a function of wavelength would be $\mu_a(\lambda) = C \times \varepsilon(\lambda)$, where C is the concentration and ε is the extinction coefficient of the chromophore at that wavelength. If the chromophores do not interact, the final absorption spectrum is a linear combination of the component spectra, and we may solve the equation by adjusting μ_a and C into the appropriate vectors, λ_1 into a matrix, and solving the matrix equation.

INSTRUMENT

The broadband DOS system consists of two separate components: steady-state spectroscopy and FDPM integrated into a single probe handpiece illustrated in figure 13.2. This probe combines steady-state and FDPM systems by crossing their source–detector paths. Thus, the volume of sample interrogated by each is nearly identical.

Two broadband instruments that differ slightly in their FDPM source components were used in this work. Each FDPM subsystem uses six to nine laser diodes (instrument 1: 672, 780, 807, 852, 896, and 913; instrument 2: 663, 680, 783, 806, 816, 855, 911, 945, and 973). The basic system schematic is shown in figure 13.2.

Diode powers (measured at the source) range between 20 and 100 mW, with the exception of diodes in the upper 900-nm region, which may have powers up to 1 W. Current and temperature control are maintained by a laser power supply. During a measurement, each laser diode is sequentially selected and intensity modulated. The AC modulation to the laser diodes is provided by a network analyzer, which sweeps through frequencies between 100 to 700 MHz. The network analyzer's radiofrequency (RF) output is coupled to the correct diode via an RF switch. A bias T circuit at each diode mixes the AC signal with DC power provided by the laser power supply.

Each diode is pigtailed to a 100-μm graded-index or coupled to 400-μm step-index fibers. Switching between the diodes is accomplished with either a multiplexed optical switch or keeping nonselected diodes below lasing current (instrument 2). Output fibers are bundled together and terminate at the handheld probe, where optical power ranges from 5 to 35 mW. The system characteristics have been described extensively by Pham et al. (2000).

The diffuse optical signal is received from the sample by an APD that is built into the handheld probe and is placed directly on the sample. The source fibers and APD are arranged in reflectance geometry within the probe. The RF output of the APD is directed to the network analyzer. Both amplitude depth and phase shift of the signal are recorded as a function of modulation frequency. A typical FDPM measurement cycling over all laser diodes will last 3[redacted] to 4[redacted] s.

The steady-state system consists of a source and CCD spectrometer. The source is a 100- or 150-W tungsten quartz halogen lamp. Source output is channeled to the sample using a 3-mm fiber bundle of 100-μm fibers (instrument 1) or a 5-mm liquid core light guide (instrument). The diffuse reflectance from the tissue is collected by a 1-mm optical fiber that is coupled to a spectrometer. In the case of the first set of experiments, the spectrometer

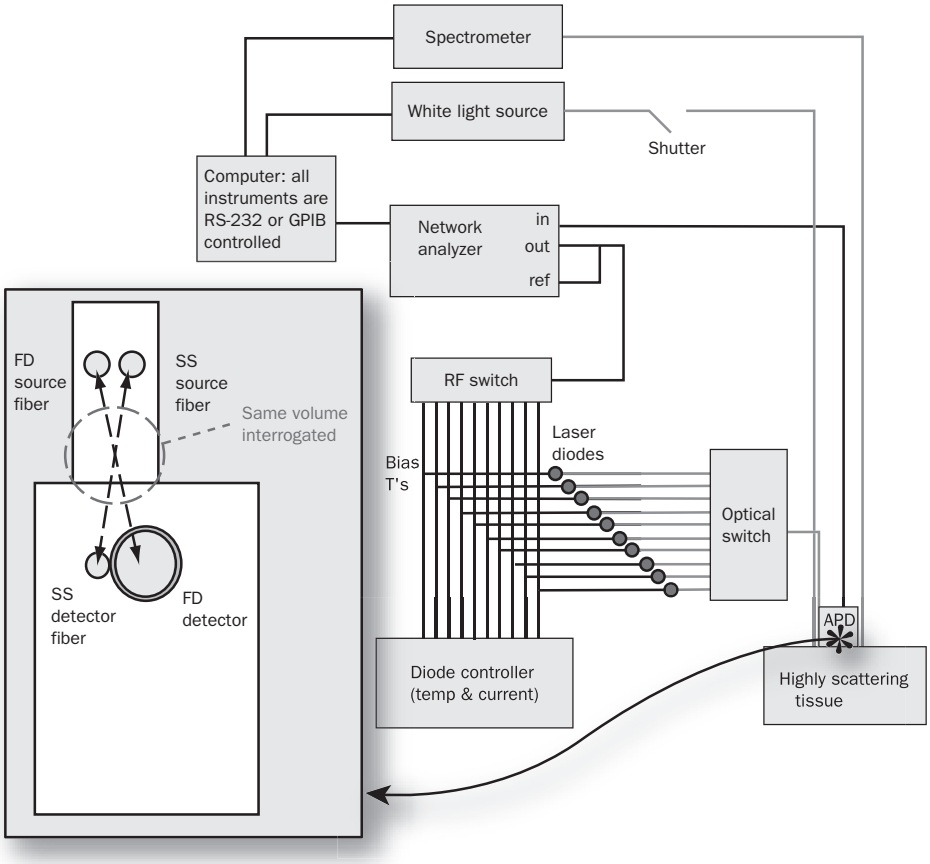

Figure 13.2 Schematic of the broadband DOS system, including the probe design on the left, which combines the steady state (SS) and frequency domain (FD) systems by crossing the interrogating paths.

uses a linear silicon CCD array with a 12-bit dynamic range. In its current configuration, the spectrometer has 5 nm spectral resolution over the 650- to 1000-nm range. Also included in the configuration is a long-pass 515-nm filter to eliminate second harmonic signals up to 1030 nm, and an L2 detector lens meant to improve light collection efficiency on the CCD. A long-pass filter at 780 nm (Schott RG-780) is partially placed in the light path to flatten the white-light response. The time required for a spectral acquisition is highly dependent on the absorption properties of the sample, varying between 15 ms to minutes. Instrument 2 uses a spectrometer with a higher dynamic range than the previous model. It contains a two-dimensional 1024×256 thermoelectrically cooled silicon CCD with a 16-bit dynamic range. Spectrometer input is provided through an SMA connection on an F/# matching optic used to optimize light collection onto the CCD. The grating chosen is blazed at 500 nm with a line density of 400 lines/mm, and the slit size is 300 μm. Also included is a long-pass glass filter with a cutoff of approximately 550 nm. Wavelength calibration was performed on a mercury–argon lamp.

The network analyzer, laser power supplies, RF switch, optical switch, and spectrometer are controlled with in-house software. Steady-state and frequency domain measurements are performed alternately to minimize the impact of laser diode and CW sources on the CCD and APD detectors, respectively. We perform a weighted, nonlinear least-squares fit using the Levenberg-Marquardt algorithm. All data fitting is done with code written in Matlab.

Materials and Methods

The samples of known scattering and absorption characteristics were made by preparing liquid phantoms from water, intralipid as the scatterer, and dye as the absorber. Intralipid is a commercially available intravenous nutritional supplement with a high-volume fraction of fatty acids (20%). Because of its negligible absorption in the 650- to 1000-nm region, it can be considered solely as a scatterer in these experiments. The scattering properties of Intralipid are published in the literature (Flock et al., 1992). Because of concern over batch-to-batch variations, we performed our own FDPM "gold standard" measurements on the Intralipid in infinite medium geometry using multiple distance calibration. These data matched surprisingly well with original published values for 20% Intralipid by van Staveren et al. (1991) with an error of less than 2% within the 650- to 1000-nm region.

The dye used in the validation measurements was copper phthalocyaninetetrasulfonic acid (CPTA; Aldrich 27,401–1, St. Louis, Missouri) prepared in a stock water-based solution. The molar extinction spectrum of the dye (ε vs. λ) was obtained using a standard spectrophotometer by measuring absorbance, A, at various concentrations, C. Using Beers law, $\mu_a = 2.3 \times \varepsilon \times C$, where ε is the molar extinction coefficient (per mole per millimeter). The resulting extinction coefficient spectrum in the near infrared is shown in figure 13.3A.

The second set of experiments used two additional chromophores: naphthol green B (Aldrich 11,991–1) and methylene blue (Aldrich M4,490–7). Peak wavelengths in the 650- to 1000-nm region are 650 nm for CPTA (minor peak at 690), 710 nm for napthol green B, and 664 nm for methylene blue. This combination was chosen because a mixture of these probes creates absorption spectra with multiple features in the near-infrared region that add similarly to chromophores in tissue spectra. Extinction coefficient spectra of all three molecules are shown in figure 13.3. These spectrophotometer measurements were taken before the addition of Intralipid.

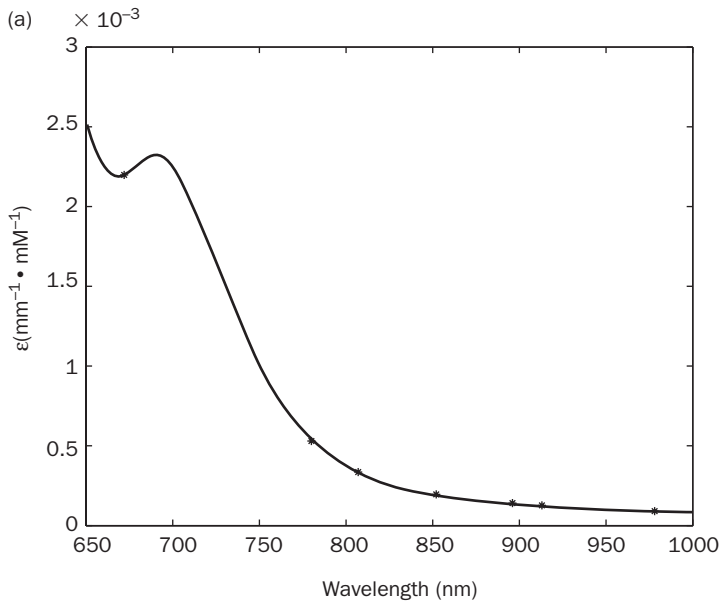

Figure 13.3 (A–C) The extinction coefficient spectra found for the dyes used in the phantoms. Asterisks mark locations of frequency domain diodes. (A) Copper phthalocyaninetetrasulfonic acid (CPTA). (B) Napthol green B. (C) Methylene blue.

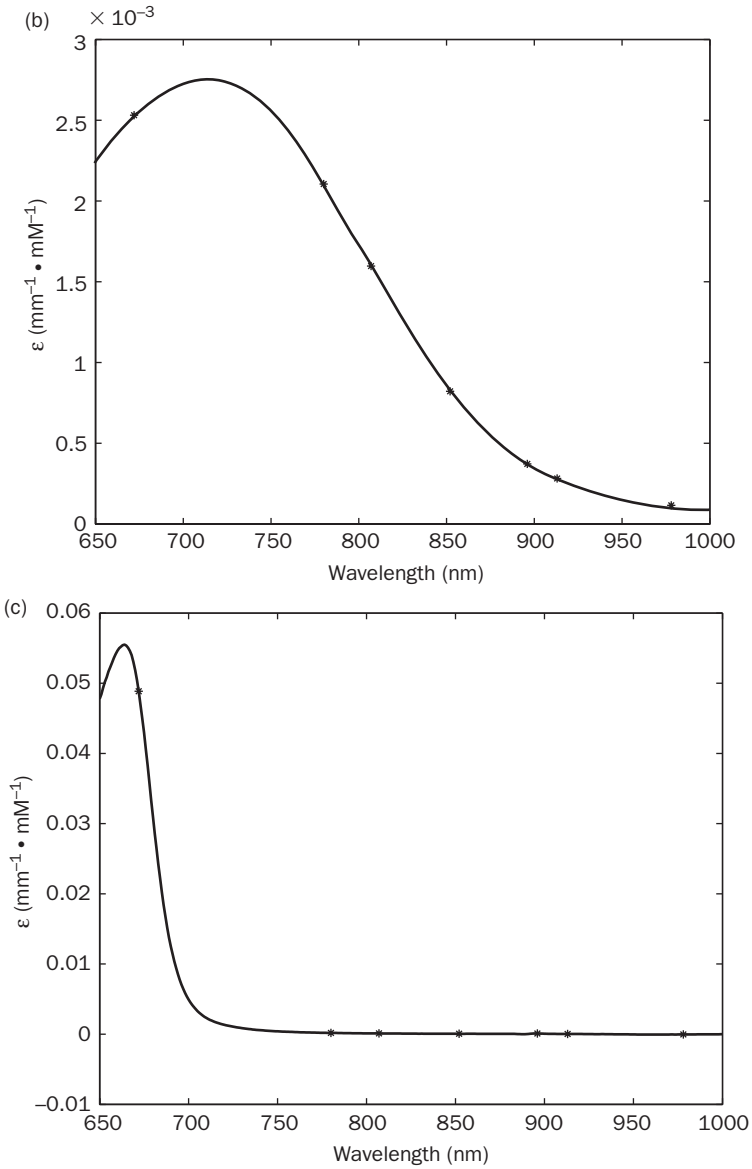

Figure 13.3 (*Continued*)

Calibration for the frequency domain system was based on a phantom of known optical properties manufactured by Medlight, SA (Lausanne, Switzerland). The optical properties of the phantom had been previously determined by multidistance, multifrequency measurements. The steady-state system was calibrated by taking source measurements in an integrating sphere coated with a material of known reflectance. Dark measurements and corrections were also made for both sets of experiments.

The liquid phantoms were prepared in a 700-mL glass beaker with a magnetic stir bar used to keep the solution homogenous. A total of 25 phantoms were prepared in the validation study and 29 were prepared in the multidye study. The probe was placed by hand onto each phantom, which was covered with thin plastic film to protect the probe from liquid. We used a source–detector separation of 20 mm in the validation studies. In the multiple-dye studies, we lengthened the separation to 24 mm because of the increased optical power

available with this particular system. Integration times were chosen to maximize the signal to at least 60% of the CCD capacity without saturating any part of the spectrum. Each phantom measurement was repeated three times.

In the validation studies, the concentrations of Intralipid and dye were chosen to span physiologically relevant μ_a and μ_s' values derived from human breast tissue measurements. The 672-nm wavelength was chosen as the representative diode. Thus, dye concentrations have a μ_a at 672 nm randomly distributed between 0.00 and 0.03/mm. Intralipid concentrations have a μ_s' at 672 nm randomly distributed between 0.2 and 2/mm.

In the multiple-dye phantoms, each dye had a concentration chosen that would randomly place the μ_a within the range of 0.0001 and 0.025/mm at its peak wavelength. After the phantom was mixed, the sum μ_a at 672 nm in fact spanned the range between 0.01 and 0.055/mm for all phantoms. In comparison, the highest μ_a we encounter in tissue within the 650- to 1000-nm range is the result of water, which at 100% concentration reaches a value of 0.05/mm at its peak wavelength ($\approx$980 nm). Most tissue measurements of μ_a fall well below this absorption.

The value for μ_s' was chosen in a similar way to that described in the validation experiments. However, the lower limit was increased to 0.5/mm to keep measurements within the diffusion approximation. The μ_s' values below the threshold of 0.5/mm had a tendency to have inverse mean free path lengths of less than 10 times the source–detector separation (24 mm) for our μ_a values, and therefore the diffusion approximation was not valid for these conditions. The final μ_a and μ_s' space covered by both sets of phantoms (at the 672-nm wavelength) is shown in figure 13.4, demonstrating a fairly even distribution within the sampled space.

Results and Discussion

Two measurements were removed from the multiple-dye phantom study because frequency domain fits showed the data to be corrupted, likely because of insufficient contact between the probe and phantom. In addition, one phantom was entirely excluded from fits in the multiple-dye study because the raw reflectance spectrum was corrupted by a shutter delay.

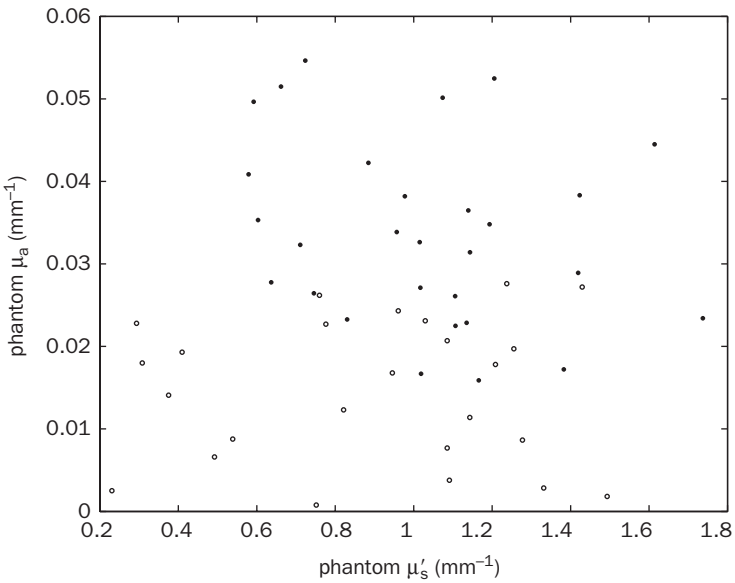

Figure 13.4 Range of μ_a and μ_s' space covered by Intralipid dye liquid Phantoms at a wavelength of 672 nm.

Figure 13.5 shows an example of the fits obtained from the first set of phantoms (single dye). In figure 13.5A, the μ_s' values are shown along with their power law fit. The fit matches closely to the original values. The power law fit is used with the steady-state reflectance to determine the μ_a spectrum. This broadband DOS-derived μ_a spectrum, along with the FDPM-derived μ_a spectrum and the dye + water fits to both, are shown in figure 13.5B.

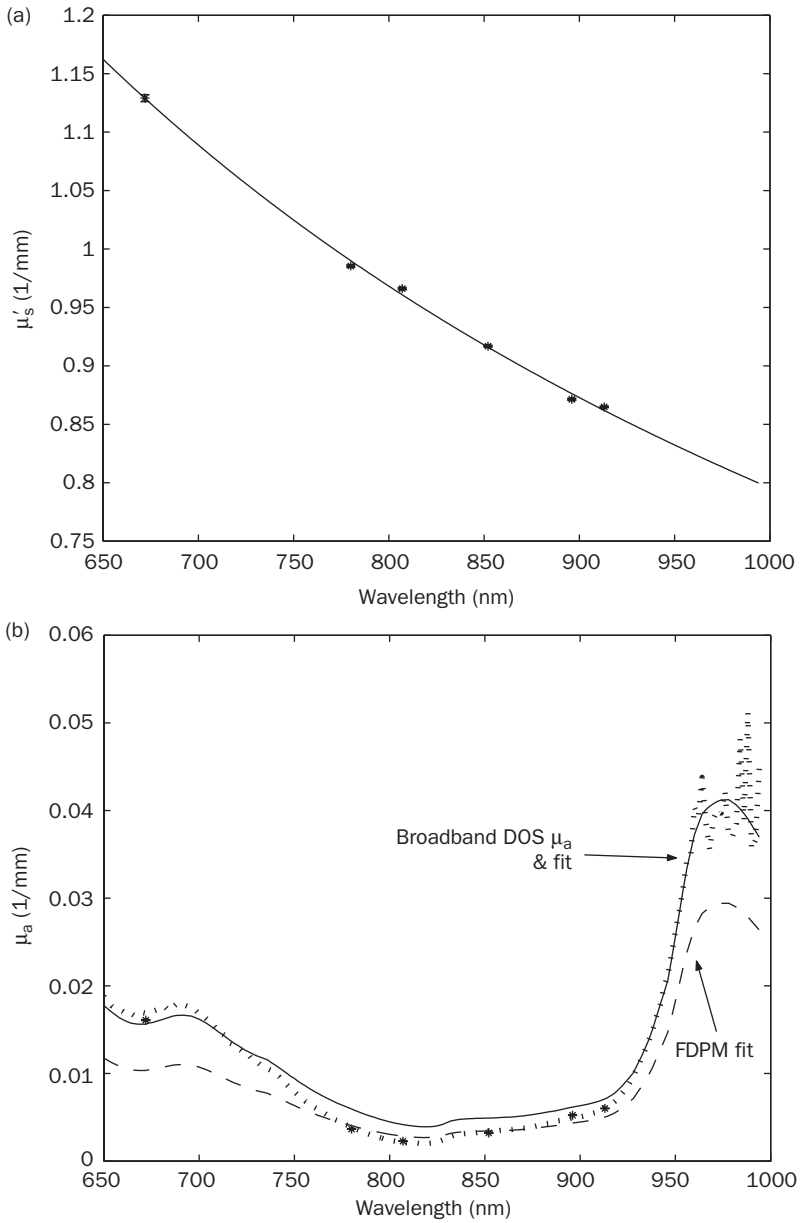

Figure 13.5 Single-dye phantoms. (A) An example of a μ_s' fit (line) to the FDPM μ_s' values (asterisks) for one of the validation phantoms. (B) The broadband DOS-derived μ_a spectrum (dotted line) is shown, along with the FDPM-derived μ_a values (asterisks). The broadband DOS-derived spectrum correlates well with the FDPM-derived μ_a values. However, the fits to the two systems are also shown (broadband DOS, solid line; FDPM. dashed line), and these differ. This example did not add a constant to the chromophore fits.

The DOS-derived spectrum correlates well with the FDPM-derived values; however, the fits to the two systems differ considerably, suggesting discrepancies between the FDPM- and broadband DOS-derived concentrations.

The results of the single-dye, or validation, set of experiments is best shown by comparing final dye concentrations. Obtained versus predicted dye and water concentrations are plotted to establish the accuracy of broadband DOS for a wide range of dye concentrations. Lipid was not fit because of its near-negligible contribution (1%) to the phantoms. Figure 13.6A displays predicted versus obtained CPTA concentrations. We also took standard spectrophotometer readings of all phantoms (sampled before the Intralipid was added). The concentrations determined by the spectrophotometer (vs. predicted values) are also plotted in figure 13.6A. These spectrophotometer values give us some indication of the error inherent in the experimental setup, including the error in mixing in the phantoms. An ideal fit would lie along the 1:1 line. Although the spectrophotometer values have a small and uniform error throughout the CPTA concentration range, both FDPM- and DOS-derived CPTA values begin to deviate considerably at higher concentrations. Frequency domain photon migration-derived values deviate significantly more than those obtained by broadband DOS.

Predicted versus obtained water volume fraction values are shown in figure 13.6B. Because the phantoms are almost completely water, all obtained values should be near 99% to 100%. Although FDPM-derived values deviate by as much as 40% from the true value, broadband DOS confers a modest improvement in accuracy, with a maximum deviation of 30%. Broadband DOS also produces a narrower range of values (≈70%–110%) than FDPM (≈60%–130%).

In figure 13.7, a flat baseline is added as a chromophore in the fit. Both broadband DOS and FDPM methods are able to recover the CPTA concentration and water volume fraction more accurately. Broadband DOS is capable of faithfully quantifying CPTA throughout the entire range of CPTA concentrations tested (fig. 13.7A). The variation seen is very similar to that of the spectrophotometer-derived values. Of note, FDPM-derived CPTA values still deviate at high CPTA concentrations. Most likely, this is the result of the deterioration of the 672-nm diode signal at higher CPTA concentrations.

With the added baseline, the water volume fraction is better recovered by both broadband DOS and FDPM (fig. 13.7B). Diffuse optical spectroscopy-derived values continue to underestimate water in most cases, whereas FDPM now overestimates it. From the raw data (not shown), the part of the μ_a spectrum that drives the water concentration (950–1000 nm) is clearly near the noise floor. Such a problem with water is only seen when there is an extremely high volume fraction, a condition that is not generally observed in tissue measurements.

Results from the second set of phantoms made with multiple dyes are shown in figures 13.8 through 13.11. This set was made to be more challenging for both FPDM and broadband DOS methods. Figure 13.8 shows an example of the fits derived with this set. Because the dye absorption was significantly higher in this set of data, FDPM phase and amplitude data were often unable to provide a satisfactory signal-to-noise ratio. This was especially true of four of the diodes (663, 680, 945, 973 nm). Because these data were often not salvageable, a condition was written into the fit that would exclude from further fitting those diodes that have modulation amplitudes below a specified level—in this case, –40 dB. Figure 13.8 shows all FDPM- and DOS-derived values, including those FDPM-derived values not used in broadband DOS fitting. In this particular example, the μ_a and μ_s' values of the two highest wavelength diodes were not used in fits, but are shown in the figures as black asterisks. The μ_s' fit in figure 13.8A shows much better correlation to original FDPM-derived μ_s' values without the inclusion of these last two diodes. There is also much better correlation between the DOS-derived μ_a spectrum and the FDPM-derived μ_a values under the same condition. Notice, however, that the FDPM-derived μ_a fit using only the best FDPM diodes

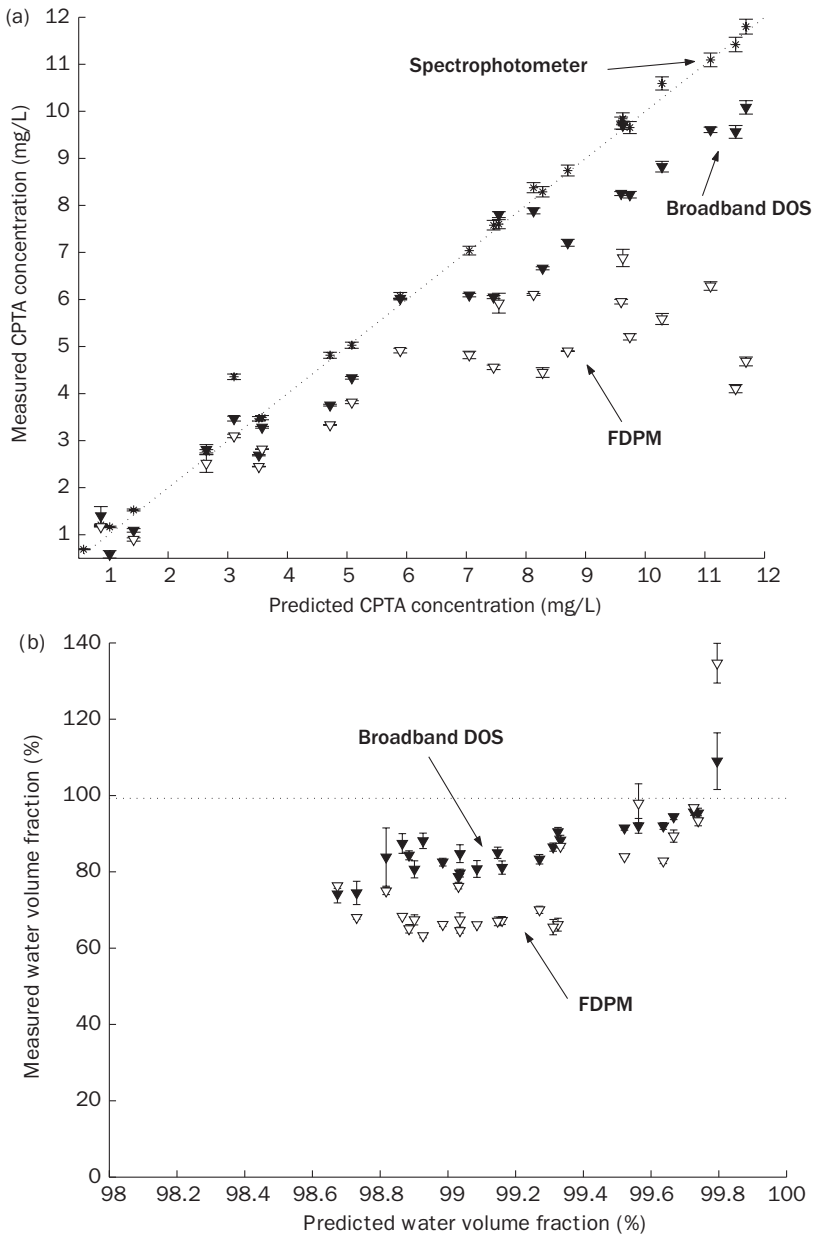

Figure 13.6 (A, B) Single-dye phantom concentrations, no baseline added. Predicted versus measured CPTA concentration (A) and water volume fraction (B) using broadband DOS (filled triangles), FDPM (open triangles), and a standard spectrophotometer (asterisks). Both values deviate from true values (1:1 dotted line). However, FDPM-derived values deviate considerably more than broadband DOS-derived values.

significantly underestimates the water μ_a contribution in the 950- to 1000-nm region and also incorrectly predicts dye μ_a contributions (as predicted by the broadband DOS μ_a spectrum) in the low 600-nm region. This is unsurprising because the lost FDPM data are in important peak regions. Thus, μ_a fits to FDPM data are not tolerant of the removal of diodes if these diodes are in a critical region. Unfortunately, this is frequently the case,

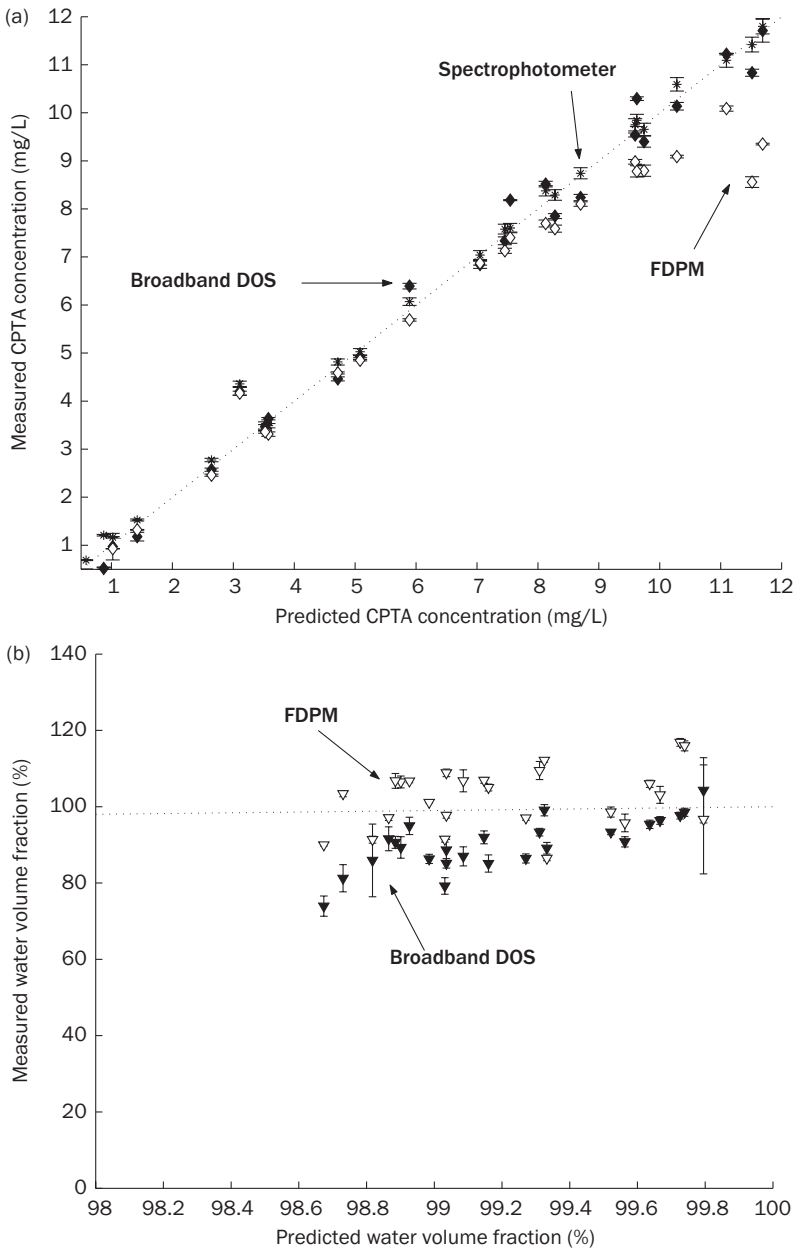

Figure 13.7 (A, B) Single-dye phantom concentrations, with baseline added. Predicted versus measured CPTA concentration (A) and water volume fraction (B) using broadband DOS (filled triangles), FDPM (open triangles), and a standard spectrophotometer (asterisks). A flat baseline was added as a chromophore to the water and CPTA fit. Copper phthalocyaninetetrasulfonic acid is recovered faithfully over the entire range by broadband DOS, whereas FDPM values deviate at higher concentrations. Water volume fraction values still contain a large degree of variation for both methods.

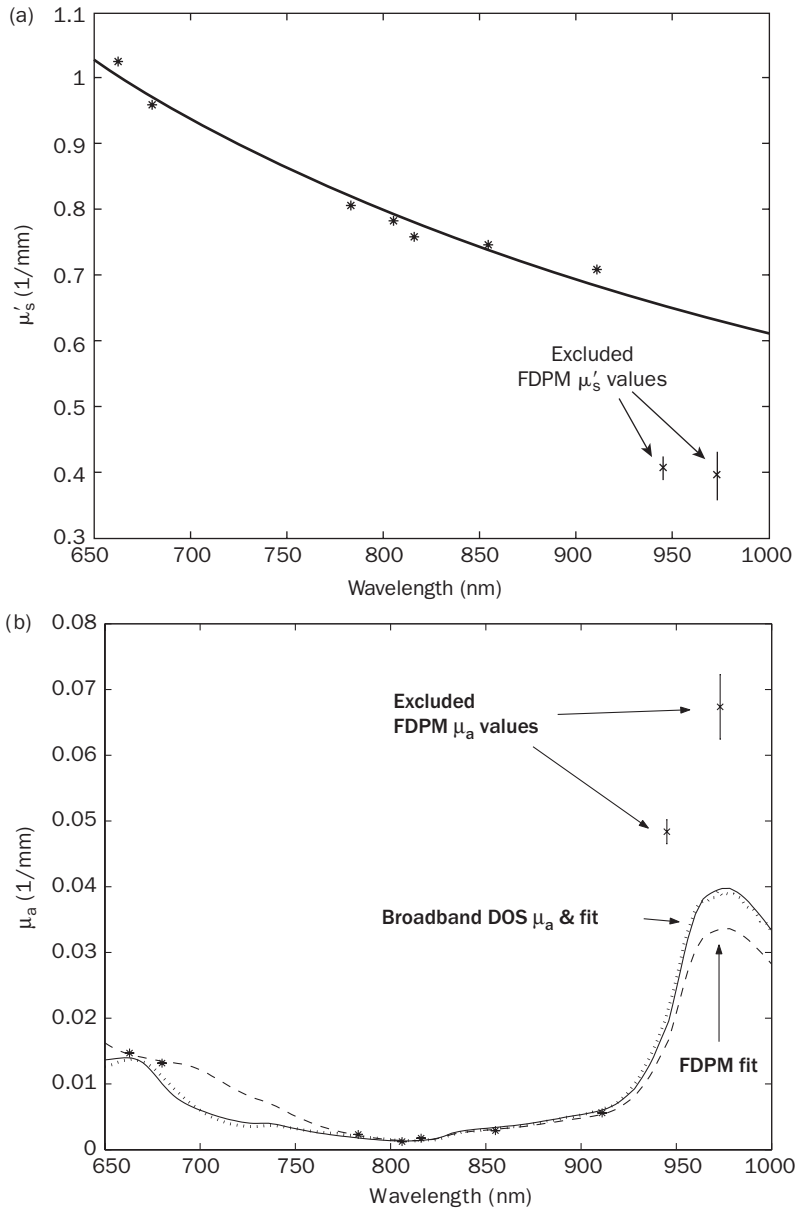

Figure 13.8 Multiple-dye phantoms. (A) An example of μ_s' fit (line) to the FDPM μ_s' values (asterisks) for one of the multiple-dye phantoms. (B) The broadband DOS-derived μ_a spectrum (dashed line) along with the FDPM-derived μ_a values (asterisks). In both views, the crosses mark FDPM-derived μ_a or μ_s' values that were thrown out before fitting. Notice that it is very difficult to get a good μ_a fit to the frequency domain-derived values (dashed line), especially if we disregard key diodes. The broadband DOS μ_a fit, however, does very well (solid line).

because attenuated signal at a particular diode wavelength is usually the result of a high concentration of a relevant chromophore.

In the multiple-dye measurements, absolute dye concentrations could not be accurately determined because the dyes interacted, changing the effective extinction coefficients. Consequently, these results were compared with spectrophotometer results, shown later.

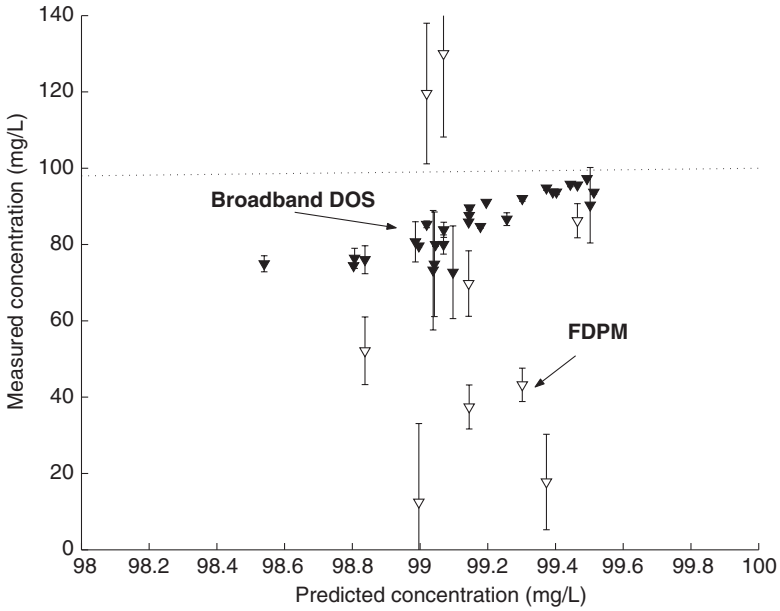

Figure 13.9 Multiple-dye phantom water concentration, with baseline added. Shown are the expected versus obtained water concentrations from the multiple-dye phantoms using broadband DOS (filled triangles), FDPM (open triangles), and a standard spectrophotometer (asterisks). The FDPM system had a difficult time recovering water concentrations under the experimental conditions, whereas the broadband DOS system was able to recover water values with the same accuracy as in the validation phantoms.

It was possible, however, to compare expected versus obtained water concentrations for the multiple dye phantoms (fig. 13.9). Comparison with results in the one-dye phantom experiments using the Ocean Optics spectrometer, shown in figure 13.7B, reveals that water values fall in the same range. At first pass these results are surprising, because the more sensitive Oriel spectrometer used in the second set of phantoms should improve the capability of the system to extract the true water concentrations, even at highly attenuating (100% water fraction) values. However, the second set of phantoms presented a very difficult set of conditions. This is quite apparent if one compares the FDPM-derived water values derived in the multiple-dye phantoms with those in the single-dye phantoms (figs. 13.9 and 13.7B). The FDPM system had a difficult time providing any meaningful data. Frequency domain photon migration-derived water values now range from 10% to 130%, whereas DOS-derived values remain in the 70% to 100% range. The broadband DOS measurement with the Oriel spectrometer was able to provide meaningful data when FDPM alone would have failed. We find this an extremely desirable feature, especially in tissue measurements.

To evaluate the multiple-dye phantom results, we obtained full absorption spectra of each phantom's dye composition (in the absence of intralipid) using the spectrophotometer. Each spectrum was converted to μ_a and corrected for the volume difference of Intralipid, which had been added after the spectrophotometer sample was taken. The known μ_a contribution of the water and lipid spectra were then added to each phantom spectrum. Therefore, each spectrophotometer-derived spectrum is a combination of measured and expected data. To test the ability of broadband DOS to reproduce the μ_a spectrum faithfully in a highly scattering medium, each spectrophotometer-derived μ_a spectrum was compared with that obtained by the broadband DOS method. Two examples of such comparison are shown in figure 13.10. The baseline of the broadband DOS-derived μ_a spectrum was allowed to

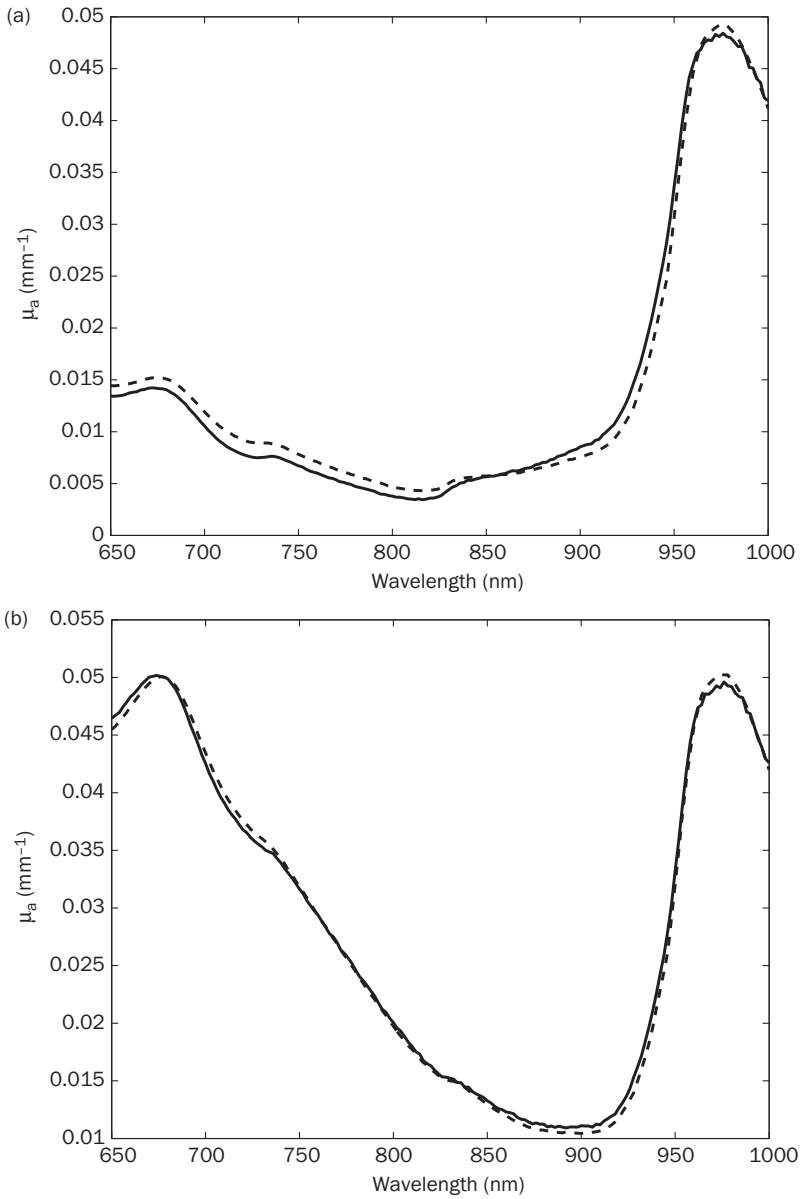

Figure 13.10 (A, B) Shown are μ_a spectra from two multiple-dye phantoms. One spectra was obtained using broadband DOS (solid) and the other was obtained from the spectrophotometer (dashed; with expected water and lipid contributions added).

vary, as was indicated by the results of the one-dye phantoms. The spectrophotometer- and DOS-derived spectra show very good correlation in both panels.

We then subtracted the spectrophotometer spectra from the broadband DOS-derived spectra to obtain residuals for all phantoms. These are shown in the figure 13.11B. In figure 13.11A, we also show all obtained spectra for the multiple-dye phantoms. In no area of the spectrum was the difference between spectra greater than 0.007/mm. This is comparable with the original resolution of the FDPM system, which in our experience has an error of approximately 0.005/mm in μ_a. We conclude that the broadband DOS system is capable

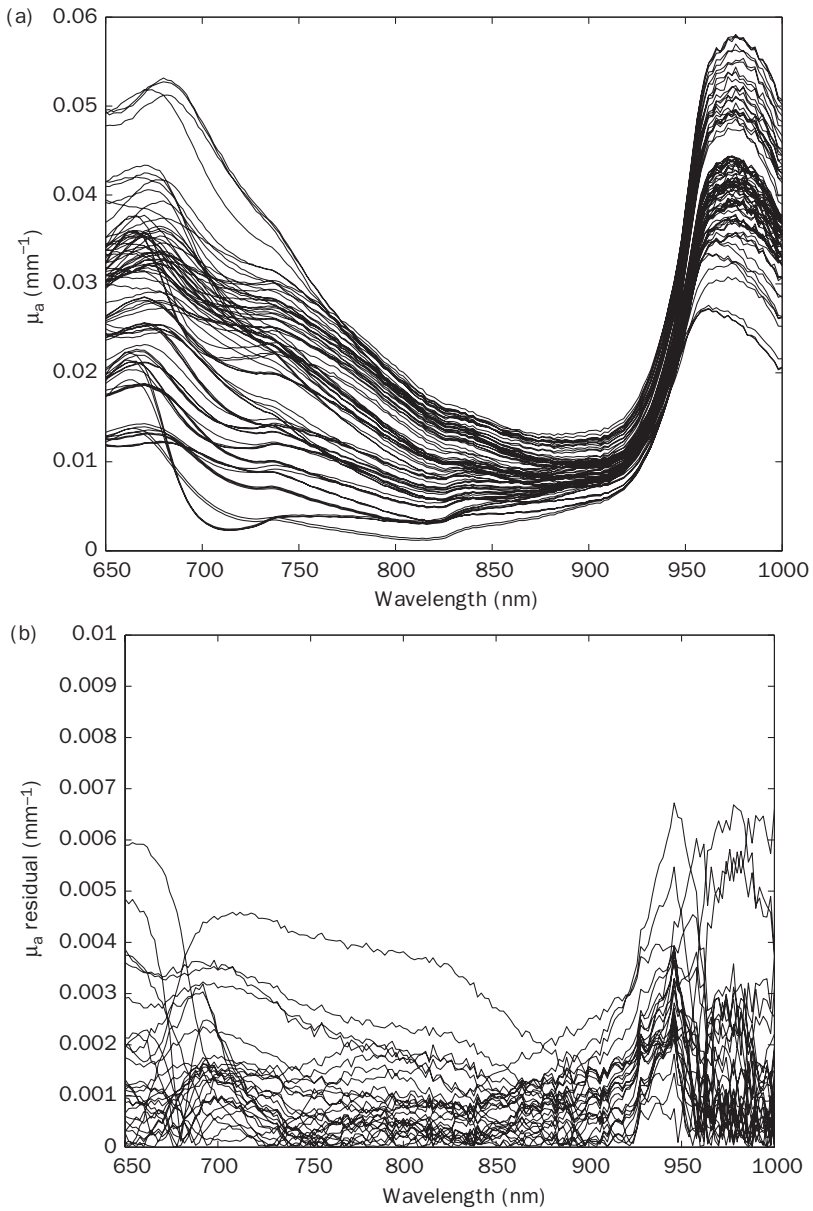

Figure 13.11 (A, B) From the multiple-dye phantoms, the final broadband DOS-derived μ_a spectra and final μ_a residuals obtained from subtracting spectrophotometer-derived spectra from broadband DOS-derived spectra. In no area of the spectrum was the difference between spectra greater than 0.007/mm.

of providing comparable accuracy in μ_a values as the FDPM system, with an added level of robustness in spectral regions of high absorption.

Summary

The combination of steady-state and FDPM is a promising approach for quantifying absorption and scattering in turbid media. The combined method, broadband DOS, consistently performs at least as well as FDPM methods alone. Diffuse optical spectroscopy can enhance

the accuracy of FDPM when discrete wavelength methods fail because of high attenuation at key diode wavelengths, (e.g., for high chromophore concentrations). Multiple-dye studies demonstrate that broadband DOS is capable of faithfully reproducing μ_a spectra in highly scattering media to within 0.007/mm if a baseline is introduced. Overall, the broadband DOS technique is capable of meeting or exceeding the accuracy of FDPM in an ideal, single-component system under high-absorption conditions in which frequency domain measurements would normally fail.

BROADBAND DIFFUSE OPTICAL SPECTROSCOPY IN MUSCLE

There have only been a few reports focused on monitoring exercised-induced changes within muscle using quantitative DOS methods (Quaresima et al., 2000; Cooper and Angus, 2003; Miura et al., 2003; Torricelli et al., 2004). In these previous studies, the primary aim was to measure the concentrations of oxyhemoglobin and deoxyhemoglobin using two wavelengths between 650 nm and 850 nm. Although wavelengths in this region are sensitive to blood absorption, they are not spectrally sensitive to water and lipid components in tissue that have high absorption in the 900- to 1000-nm region.

Figure 13.12 shows absorption spectra of oxyhemoglobin, deoxyhemoglobin, water, and lipid—the main chromophores within tissue in the 650- to 1000-nm spectral region. By simply examining the characteristic shapes and the chromophore absorption spectra, it is obvious that water and lipids contribute very little to the tissue absorption below 900 nm. In this section we present results of broadband DOS measurements on human muscle that demonstrate sensitivity to water and lipid that would otherwise be impossible to recover with a standard two- to four-wavelength tissue oximeter. We present these results to highlight two important features: (1) the sensitivity of broadband DOS to subtle physiological changes in muscle and (2) the opportunity for broadband DOS to provide new information on subcutaneous fat layers.

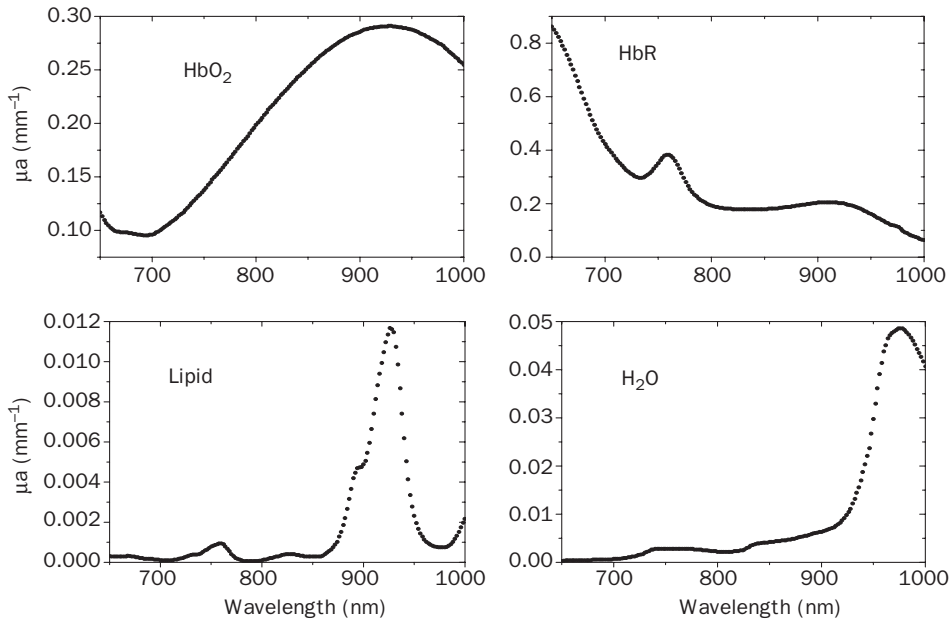

Figure 13.12 Absorption spectra plotted for major absorbers in tissue. Oxyhemoglobin (HbO_2), 1 mM; deoxyhemoglobin (HbR), 1 mM; lipid, 0.9 g/cm^3; H_2O, 1 g/cm^3.

Materials and Methods

The broadband DOS system used for muscle measurements was nearly identical to the system described in the phantom validation section; the only differences were the broadband light source (Ocean Optics LS-1) and the specific laser diode wavelengths. For the muscle measurements, a total of five laser diodes were used at the following wavelengths: 658, 785, 810, 830, and 850 nm.

Measurements were carried out one male volunteer (age, 26 years; weight, 160 lb; height, 188 cm), using approved University of California at Irvine human subjects protocol 2001-1924, who was not participating in any type of strength-training regimen. A single location was chosen at the center of the subject's two biceps brachii, allowing for repeat measurements of the same tissue volumes. Ultrasound was used to measure skin/fat layer thicknesses of 0.16 and 0.17 cm for the right and left arms, respectively, at the measurement locations. The source–detector separation used in the study was 2.1 cm, which allowed for sufficient light penetration into the muscle given the relatively thin top layer thickness measured.

Initially, five baseline measurements were taken on each arm, with the axis that bisected the source and detector oriented along the length of the muscle fibers. The subject's nondominant biceps brachii (left arm) was then exercised by repeatedly curling a 20-lb weight until failure. This was followed by negative curls during which the subject was helped to lift the weight and then asked to apply resistance as it was pulled down by gravity (10 repetitions). The total time elapsed during exercise was 4 minutes and the acquisition of postexercise measurements began within 30 s of exercise completion. Three measurements were then taken on the exercised arm followed by a single measurement on the nonexercised arm; this sequence of measurements was repeated until a total of 48 postexercise measurements had been acquired from the exercised arm and 16 from the nonexercised arm. The total time spent on postexercise measurements was just over 1 hour (1:03:20) with an average measurement time of 60 s. The data were processed three separate ways to allow a comparison between broadband DOS and DOS alone. For broadband DOS, the entire absorption spectrum was determined using all five laser diodes plus the broadband information. A chromophore fit was then performed using the extinction coefficients of deoxyhemoglobin, oxyhemoglobin, water, lipid, and a flat baseline. To allow for a comparison with broadband DOS, extinction coefficients of deoxyhemoglobin, oxyhemoglobin, and a baseline were fit to the absorption coefficients determined at the five laser diode wavelengths only, whereas water and lipids were assumed not to contribute significantly to the absorption spectrum in this region. This provided concentrations of deoxyhemoglobin and oxyhemoglobin determined only from the frequency domain measurements. Last, water, lipid, hemoglobin, oxyhemoglobin, and a baseline were all fit to the absorption coefficients at the five laser diode wavelengths to acquire water and lipid concentrations that could be compared directly with those recovered using broadband DOS.

Results and Discussion

Figure 13.13 is a plot of a typical μ_a spectrum measured on the arm of the volunteer. The fit of the chromophore spectra (deoxyhemoglobin, oxyhemoglobin, water, lipid, and a constant background absorption) to the μ_a spectrum allows for the determination of the concentrations and is described in detail later. The figure shows a qualitatively good fit of the chromophore spectra to the measured μ_a spectrum. The muscle spectra also illustrate how well the endogenous chromophore features stand out, particularly the water peak (978 nm) and the deoxyhemoglobin absorption at lower wavelengths. Notice that the lipid peak is not visually apparent in this measurement because the fat layer thickness of this subject was

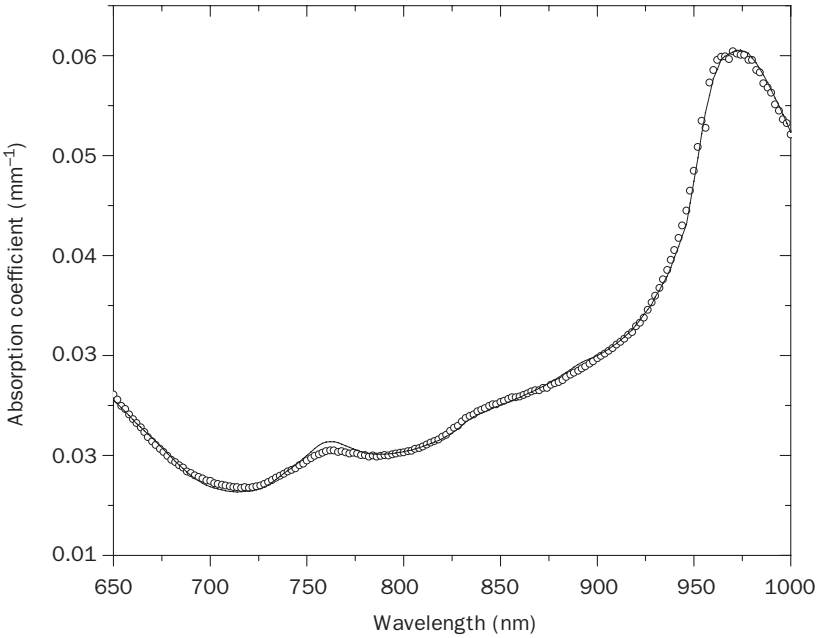

Figure 13.13 Measurements of tissue spectra using DOS. Circles, μ_a muscle spectrum measured with broadband DOS instrument. Solid curve, fit of deoxyhemoglobin, oxyhemoglobin, water, lipid, and baseline absorption spectra to measured μ_a spectrum.

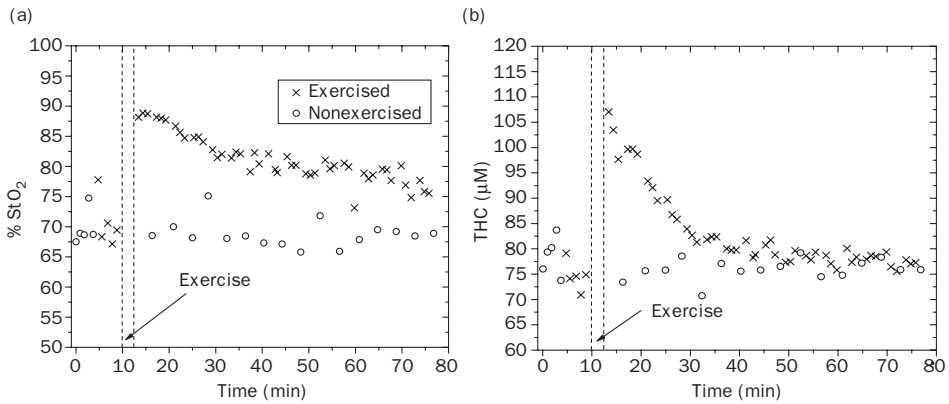

Figure 13.14 (A, B) Tissue oxygen saturation (StO_2; A) and total hemoglobin content (THC; B) recovered from muscle measurements on the volunteer's exercised (x) and nonexercised (o) arms. The exercise period is represented by time between dashed vertical lines.

minimal. This lipid peak is obvious in tissues with higher lipid content, such as breast, or in individuals with thicker subcutaneous fat layers.

Figure 13.14 is a plot of the tissue oxygen saturation (StO_2) and total hemoglobin content (THC) measured on both the exercised arm and the nonexercised arm over 70 minutes.

Tissue oxygen saturation is an indicator of local tissue metabolism, and is defined as the following:

$$StO_2 = \frac{HbO_2}{HbR + HbO_2}$$

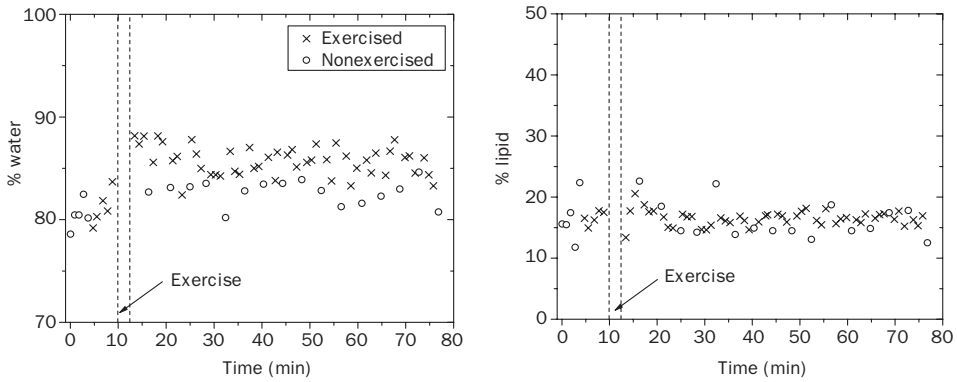

Figure 13.15 (A, B) Water (A) and lipid (B) recovered from muscle measurements on the volunteer's exercised (x) and nonexercised (o) arms. The exercise period is represented by time between dashed vertical lines.

Both StO_2 and THC increase significantly in the exercised arm immediately after exercise, with THC returning close to baseline within 25 minutes. The StO_2 value also demonstrates a fast return to baseline within the first 20 minutes and tapers off to a slower ~~decent~~, but StO_2 values continue to remain elevated from baseline 60 minutes after exercise. The recovered THC and StO_2 values for the nonexercised arm show no significant changes before and after exercise.

Figure 13.15 is a plot of the water content and the lipid content of both the exercised (x) and nonexercised (o) arms. There is a modest increase in the water values measured on the exercised arm immediately after exercise (8%), and these values remain elevated from baseline 60 minutes later. The nonexercised arm also shows a statistically significant increase in water before and after exercise, although not as high (3%) as the increase in the exercised arm. As expected, there are no exercise-induced changes in the lipid content of either arm.

The results using only the five laser diodes without the broadband measurement provide similar trends in blood values, with lower contrast between the pre- and postexercise measurements in recovered oxyhemoglobin concentrations. Table 13.1 lists the percentage change between the first three postexercise measurements and the five preexercise measurements. Looking directly at the deoxyhemoglobin and oxyhemoglobin concentrations, it is apparent that the changes in deoxyhemoglobin are nearly the same without the broadband measurement. On the other hand, the contrast between pre- and postexercise measurements of oxyhemoglobin is greatly reduced when the broadband measurement is eliminated. This is a result of two observed differences: The average concentration recovered for oxyhemoglobin at baseline is increased by 30 μM and the absolute change in oxyhemoglobin resulting from exercise is reduced from 40 μM to 20 μM when the broadband measurement is neglected. The absorption spectra plotted in figure 13.12 provide some explanation for these results. The deoxyhemoglobin spectrum is strongly absorbing in the spectral region between 650 and 850 nm, and also has very distinct spectral features, such as the peak at 758 nm. The laser diodes used do a good job of sampling this spectral region. Therefore, the recovered deoxyhemoglobin concentrations preserve the contrast between the pre- and postexercise measurements with and without the broadband measurement, although there are still differences in the absolute concentrations recovered.

In contrast, the absorption spectrum of oxyhemoglobin is much smoother and has a maximum absorption at 929 nm. Because the oxyhemoglobin spectrum lacks distinct features, it may require the increased spectral content from the broadband measurement to fit accurately

Table 13-1. Percent difference between five baseline measurements and three postexercise measurements on muscle.

Chromophore	Percent change, broadband DOS (exercised)	Percent change, broadband DOS (nonexercised)	Percent change, ~~DOS~~ 1 only (exercised)	Percent change, ~~DOS~~ 1 only (nonexercised)
Oxyhemoglobin	$+72 \pm 19$	-6 ± 8	$+29 \pm 4$	$+5 \pm 4$
Deoxyhemoglobin	-46 ± 7	-2 ± 7	-45 ± 9	-4 ± 10
Total hemoglobin content	$+37 \pm 8$	-5 ± 5	$+12 \pm 3$	$+2 \pm 2$
Tissue oxygen saturation	$+25 \pm 7$	-1 ± 4	$+15 \pm 3$	$+2 \pm 3$
Water	$+8 \pm 2$	$+3 \pm 2$	$+58 \pm 70$	-6 ± 38
Lipid	$+4 \pm 23$	$+12 \pm 36$	$+485 \pm 1040$	-88 ± 170

The first two columns include the broadband DOS measurements on the exercised and nonexercised arms respectively. The last two columns are the same for values derived from the five wavelength frequency domain data. Errors are represented by the standard deviations determined from repeat measurements.

for this concentration. Ultimately, this reduced sensitivity to oxyhemoglobin decreases the sensitivity of both StO_2 and THC recovered without the broadband measurement.

As expected, the water and lipid concentrations recovered without the broadband measurement have large errors and are meaningless because the wavelengths used are not sensitive to the regions where these chromophores are the dominant absorbers. When water is fit using the broadband measurement, it provides the highest precision of all the chromophores recovered. This is because water is not only highly absorbing, but it is also highly concentrated within tissue. The lipid measurements, on the other hand, have the largest error of all the chromophores, which is a result of their lower concentrations in the subject's arm and lower absorption compared with water and oxyhemoglobin. Despite the higher measurement errors, the recovered lipids are within a range that is anatomically correct and are unchanging during the time course of the measurements.

Summary

These results have been presented to demonstrate the capabilities of broadband DOS to measure physiological changes within muscle after exercise. An important feature of this measurement is the sensitivity of DOS to changes in muscle water content that are difficult to observe. These alterations may provide insight into conditions such as muscle soreness, muscle injury, and compartment syndromes that could follow from tissue damage and edema. We also measure substantially different absolute concentrations of oxyhemoglobin with and without the broadband measurement included (53 ± 3 μM and 84 ± 4 μM, respectively). Although we do not have the absolute chromophore values for a comparison, we can use the phantom measurements presented in the previous section as a validation of broadband DOS accuracy. This improved accuracy has important implications for estimation of commonly used metabolic indices such as THC and StO_2.

BROADBAND DIFFUSE OPTICAL SPECTROSCOPY IN BREAST TISSUE

Near-infrared optical mammography has only recently become clinically feasible as a result of significant improvements in optical detectors, sources, and components, coupled with important advances in the understanding of the interaction between light and tissue. Near-infrared spectra are sensitive to several important physiological components in tissue such as oxyhemoglobin, deoxyhemoglobin, water, and lipids. In the clinical management of breast

disease, such functional information suggests a variety of potential medical applications: therapeutic monitoring (angiogenesis, chemotherapy), supplemental lesion characterization (benign vs. malignant), and risk assessment (origins of mammographic breast density). A noninvasive optical imaging technique that provides unique, quantitative physiological information can greatly enhance current screening and diagnostic monitoring for the breast.

Results and Discussion

Many groups have demonstrated that increasing the spectral bandwidth of optical mammography improves tissue functional characterization (Pera et al., 2003; Pifferi et al., 2003; Srinivasan et al., 2003). An example of this is illustrated by point broadband DOS measurements acquired on a 54-year-old human subject with an ≈2-cm-diameter adenocarcinoma ≈1 cm beneath the breast surface (fig. 13.16). Measurements were performed according to University of California at Irvine–approved human subjects protocol 95–563. The tumor site, which represents an average of both normal and diseased tissue, displays increased absorption in the 650- to 850-nm spectral range, corresponding to higher THC. The pronounced peak at 750 nm represents an increase in deoxygenated hemoglobin in the tumor tissue. Additional spectral features are present at 920 nm (lipids) and 980 nm (water). The lipid-to-water ratio is substantially greater for normal tissue, indicating a significant increase in tumor water content. The components of the tissue may be quantified by fitting these absorption spectra to the assumed known basis spectra (oxyhemoglobin, deoxyhemoglobin, water, and lipids). Overall, the spectral differences between normal and tumor are manifestations of multiple physiological changes associated with increased vascularization, oxygen consumption, cellularity, and edema in the tumor-containing tissue.

However, a practical concern exists. Although the broadband source permitted a detailed tissue functional profile, it is difficult to generate rapid breast images using our current broadband DOS method as a result of (1) slow acquisition times and high number of wavelengths required by FDPM, and (2) long integration times required by steady-state spectroscopy. Technical improvements can significantly reduce FDPM acquisition time, but problem 2 is a signal-to-noise limitation that can only be addressed by better detectors and brighter sources.

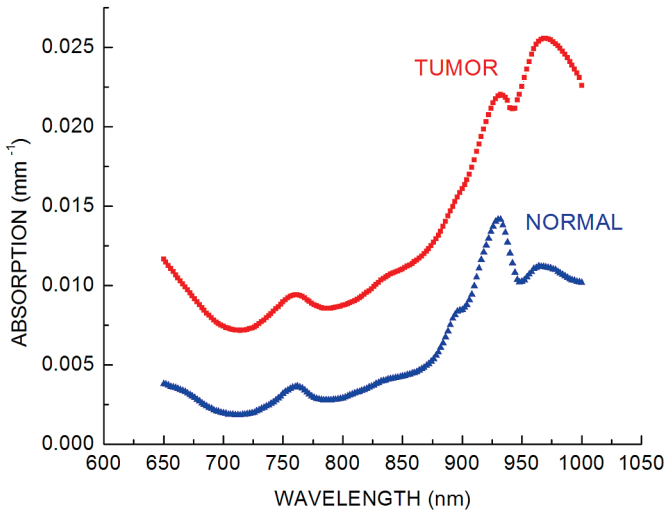

Figure 13.16 Differences between the absorption spectra of normal and tumor-containing breast tissue.

We can minimize the impact of these limitations by using features of broadband DOS to preserve the spectral content, yet decrease measurement time. Figure 13.17 presents measurements of a series of linear point broadband DOS measurements of 24 normal breasts (12 right, 12 left). Each point in figure 13.17 represents a population average of the same data, but has been processed in different ways. Error bars, which represent population variance, are not included because they do not affect the subsequent analysis. The first method (FDPM) uses nine discrete FDPM wavelengths (660, 685, 786, 809, 822, 852, 911, 946, and 973 nm). The second method (SSALL) uses the broadband DOS technique: the same

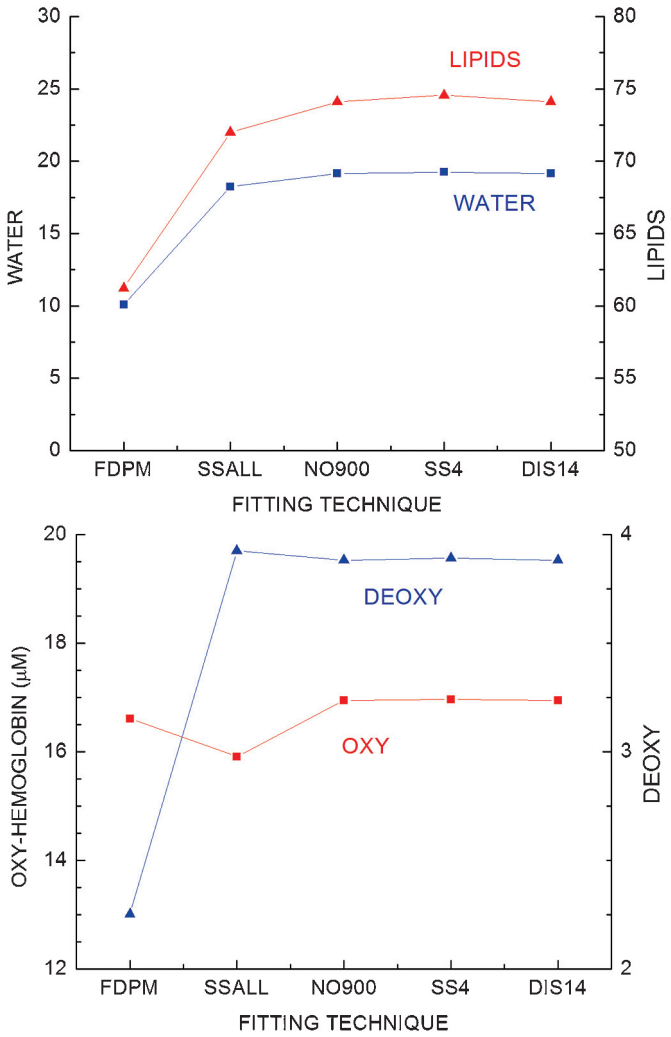

Figure 13.17 Comparison between fitting techniques using a both breasts in a population of 12 normal subjects. Each point represents a population average. The FDPM method uses only a nine-wavelength FDPM fit, whereas (SSALL) adds to this the broadband DOS spectra. NO900 is similar to SSALL, but does not use FDPM wavelengths above 900 nm. SS4 is similar to NO900, but it uses only four FDPM wavelengths instead of six. Last, DIS14 uses the same four FDPM wavelengths as SS4, and 14 steady-state wavelengths spread throughout the near infrared. Notice that all the techniques using stead-state wavelengths (SSALL, NO900, SS4, and DIS14) yield similar results.

nine laser diodes plus the broadband light source. We see that the data are consistent between the two cases, but the values of deoxyhemoglobin, water, and lipids are noticeably higher in the broadband DOS measurement. Given the results of the phantom study described earlier, we assume these broadband DOS values are a better characterization of the tissue composition than FDPM alone.

Results similar to SSALL are found by using only the six laser diodes below 900 nm along with the broadband source (NO900). The results are also seemingly unchanged by using just four common laser diode wavelengths (660, 685, 786, and 822 nm) along with the broadband source (SS4). These findings are significant because diodes above 900 nm, in our experience, are typically difficult to modulate, sometimes producing inconsistent results because of a lack of modulation depth. Notice that problems with these FDPM wavelengths were minimized by the inclusion of the broadband source in SSALL. By using only laser diodes that are easily modulated, we can drastically improve the signal-to-noise ratio of the system. In addition, we can restrict the modulated laser diodes to wavelengths at which scattering and absorption are easily separated (unlike 980 nm), an approach that has been discussed in a different light by Corlu et al. (2003).

The last case (DIS14) uses only four laser diode wavelengths (660, 685, 786, and 822 nm) and 14 steady-state discrete wavelengths (634, 652, 686, 762, 812, 822, 832, 852, 872, 882, 902, 920, 952, and 982 nm), which were taken from the broadband measurement. These discrete steady-state wavelengths were selected solely based upon commercial availability as dedicated solid-state sources. On average, the same results are obtained using this "discrete" broadband DOS approach as with any of the previous broadband DOS fitting schemes. This finding is significant because the broadband source may now be replaced by a series of discreet solid-state sources, which can generate far greater amounts of light in the selected wavelength bands than a conventional broadband lamp. Broadband integration times, which ranged anywhere from 1000 to 10,000 ms in this study, could be reduced conservatively by an order of magnitude. Thus, spectral imaging of the breast at a great number of locations becomes a practical endeavor. Image reconstructions using spectral data would only require 14 bands in this case, rather than the 300 we acquired in the full broadband DOS measurements (SSALL, NO900, and SS4).

Summary

Broadband spectroscopy enhances optical mammography by increasing contrast and providing new, physiology-based diagnostic criteria. This improved performance has usually come at great cost because it has been difficult to obtain scatter-corrected data in the 900- to 1000-nm region. However, various approaches can be used to reduce the information content of combined CW and frequency domain measurements while maintaining accuracy. For example, a limited number of discrete-wavelength frequency domain sources in the 650- to 850-nm region can be combined with broadband CW spectra. Similarly, we have seen that using a limited number of steady-state, commercially available, discrete-wavelength laser diodes can provide enough spectral content to maintain the tissue characterization capability of broadband DOS. These observations provide a technical framework that balances the requirements of imaging and spectroscopy in thick tissues.

ACKNOWLEDGMENTS

We acknowledge the National Institutes of Health (LAMMP: P41-RR01192 and NTROI: U54-CA105480), the California Breast Cancer Research Program, the Air Force Office of Scientific Research (MFEL: F49620–00–1–0371), the Beckman Foundation, and the University of California at Irvine Medical Scientist Training Program (D.J.) for support of

this research. Use of University of California at Irvine clinical facilities and support in the Chao Family Comprehensive Cancer Center, the General Clinical Resource Center, and the Laser Surgery Clinic is gratefully acknowledged.

REFERENCES

Adcock, L. M., L. S. Wafelman, S. Hegemier, A. A. Moise, M. E. Speer, C. F. Contant, and J. Goddard-Finegold. Neonatal intensive care applications of near-infrared spectroscopy. *Clin Perinatol* 26, no. 4 (1999): 893–903, ix.

Benaron, D. A., S. R. Hintz, A. Villringer, D. Boas, A. Kleinschmidt, J. Frahm, C. Hirth, H. Obrig, J. C. van Houten, E. L. Kermit, W. F. Cheong, and D. K. Stevenson. Noninvasive functional imaging of human brain using light. *J Cereb Blood Flow Metab* 20, no. 3 (2000): 469–477.

Bevilacqua, F., A. J. Berger, A. E. Cerussi, D. Jakubowski, and B. J. Tromberg. Broadband absorption spectroscopy in turbid media by combined frequency-domain and steady-state methods. *Appl Opt* 39, no. 34 (2000): 6498–6507.

Cerussi, A. E., A. J. Berger, F. Bevilacqua, N. Shah, D. Jakubowski, J. Butler, R. F. Holcombe, and B. J. Tromberg. Sources of absorption and scattering contrast for near-infrared optical mammography. *Acad Radiol* 8, no. 3 (2001): 211–218.

Cooper, C. E., and C. Angus. Blood volume changes are controlled centrally not locally: A near-infrared spectroscopy study of one legged aerobic exercise. *Adv Exp Biol* 530 (2003): 627–635.

Corlu, A., T. Durduran, R. Choe, M. Schweiger, E. M. C. Hillman, S. R. Arridge, and A. G. Yodh. Uniqueness and wavelength optimization in continuous-wave multispectral diffuse optical tomography. *Opt Lett* 28, no. 23 (2003): 2339–2341.

Cubeddu, R., C. D'Andrea, A. Pifferi, P. Taroni, A. Torricelli, and G. Valentini. Effects of the menstrual cycle on the red and near-infrared optical properties of the human breast. *Photochem Photobiol* 72, no. 3 (2000): 383–391.

Fantini, S., D. Hueber, M. A. Franceschini, E. Gratton, W. Rosenfeld, P. G. Stubblefield, D. Maulik, and M. R. Stankovic. Non-invasive optical monitoring of the newborn piglet brain using continuous-wave and frequency-domain spectroscopy. *Phys Med Biol* 44, no. 6 (1999): 1543–1563.

Fantini, S., S. A. Walker, M. A. Franceschini, M. Kaschke, P. M. Schlag, and K. T. Moesta. Assessment of the size, position, and optical properties of breast tumors in vivo by noninvasive optical methods. *Appl Opt* 37, no. 10 (1998): 1982–1989.

Farrell, T. J., M. S. Patterson, and B. Wilson. A diffusion theory model of spatially resolved, steady-state diffuse reflectance for the noninvasive determination of tissue optical properties in vivo. *Med Phys* 19, no. 4 (1992): 879–888.

Fishkin, J. B. *Imaging and Spectroscopy of Tissue-Like Phantoms Using Photon Density Waves: Theory and Experiments.* University of Illinois, Urbana-Champaign, 1994.

Flock, S. T., B. C. Jacques, B. C. Wilson, W. M. Star, and M. J. C. van Gemert. Optical properties of intralipid: A phantom medium for light propagation studies. *Lasers Surg Med* 12, no. 5 (1992): 510–519.

Franceschini, M. A., K. T. Moesta, S. Fantini, G. Gaida, E. Gratton, H. Jess, W. M. Mantulin, M. Seeber, P. M. Schlag, and M. Kaschke. Identification and quantification of intrinsic optical contrast for near-infrared mammography. *Proc Natl Acad Sci USA* 94 (1997): 6468–6473.

Giannotti, G., S. M. Cohn, M. Brown, J. E. Varela, M. G. McKenney, and J. A. Wiseberg. Utility of near-infrared spectroscopy in the diagnosis of lower extremity compartment syndrome. *J Trauma* 48, no. 3 (2000): 396–399; discussion, 399–401.

Graaff, R., J. G. Aarnoudse, J. R. Zijp, P. M. A. Sloot, F. F. M. Demul, J. Greve, and M. H. Koelink. Reduced light-scattering properties for mixtures of spherical particles: A simple approximation derived from Mie calculations. *Appl Opt* 31, no. 10 (1992): 1370–1376.

Haskell, R. C., L. O. Svaasand, T. Tsay, M. S. Feng, M. S. McAdams, and B. J. Tromberg. Boundary conditions for the diffusion equation in radiative transfer. *J Opt Soc Am A* 11, no. 10 (1994): 2727–2741.

Ishimaru, A. *Wave Propagation and Scattering in Random Media.* Vol. 1. Academic Press, [CITY], 1978.

Miura, H., K. McCully, and B. Chance. Application of multiple NIRS imaging device to the exercising muscle metabolism. *Spectroscopy* 17 (2003): 549–558.

Moesta, K. T., S. Fantini, H. Jess, M. A. Totkas, M. A. Franceschini, M. Kaschke, and P. M. Schlag. Contrast features of breast cancer in frequency-domain laser scanning mammography. *J Biomed Opt* 3, no. 2 (1998): 129–136.

Mourant, J. R., J. P. Freyer, A. H. Hielscher, A. A. Eick, D. Shen, and T. M. Johnson. Mechanisms of light scattering from biological cells relevant to noninvasive optical-tissue diagnostics. *Appl Opt* 37, no. 16 (1998): 3586–3593.

Mourant, J. R., T. Fuselier, J. Boyer, T. M. Johnson, and I. J. Bigio. Predictions and measurements of scattering and absorption over broad wavelength ranges in tissue phantoms. *Appl Opt* 36, no. 4 (1997): 949–957.

Patterson, M. S., B. Chance, and B. C. Wilson. Time resolved reflectance and transmittance for the non-invasive measurement of tissue optical properties. *Appl Opt* 28, no. 12 (1989): 2331–2336.

Pera, V. E., E. L. Heffer, H. Siebold, O. Schutz, S. Heywang-Kobrunner, L. Gotz, A. Heinig, and S. Fantini. Spatial second-derivative image processing: An application to optical mammography to enhance the detection of breast tumors. *J Biomed Opt* 8, no. 3 (2003): 517–524.

Pham, T. H., O. Coquoz, J. B. Fishkin, E. Anderson, and B. J. Tromberg. Broad bandwidth frequency domain instrument for quantitative tissue optical spectroscopy. *Rev Sci Instrum* 71, no. 6 (2000): 2500–2513.

Pifferi, A., P. Taroni, A. Torricelli, F. Messina, R. Cubeddu, and G. Danesini. Four-wavelength time-resolved optical mammography in the 680–980-nm range. *Opt Lett* 28, no. 13 (2003): 1138–1140.

Quaresima, V., S. Homma, K. Azuma, S. Shimizu, F. Chiarotti, M. Ferrari, and A. Kagaya. Calf and shin muscle oxygenation patterns and femoral artery blood flow during dynamic plantar flexion exercised in humans. *Eur J Appl Physiol* 84 (2000): 387–394.

Springett, R., M. Wylezinska, E. B. Cady, M. Cope, and D. T. Delpy. Oxygen dependency of cerebral oxidative phosphorylation in newborn piglets. *J Cereb Blood Flow Metab* 20, no. 2 (2000): 280–289.

Srinivasan, S., B. W. Pogue, S. Jiang, H. Dehghani, C. Kogel, S. Soho, J. J. Gibson, T. D. Tosteson, S. P. Poplack, and K. D. Paulsen. Interpreting hemoglobin and water concentration, oxygen saturation, and scattering measured in vivo by near-infrared breast tomography. *Proc Natl Acad Sci USA* 100, no. 21 (2003): 12349–12354.

Torricellli, A., V. Quaresima, A. Pifferi, G. Biscotti, L. Spinelli, P. Taroni, M. Ferrari, and R. Cubeddu. Mapping of calf muscle oxygenation and haemoglobin content during dynamic plantar flexion exercise by multi-channel time-resolved near-infrared spectroscopy. *Phys Med Biol* 49 (2004): 685–699.

Tromberg, B. J., N. Shah, R. Lanning, A. Cerussi, J. Espinoza, T. Pham, L. Svaasand, and J. Butler. Non-invasive in vivo characterization of breast tumors using photon migration spectroscopy. *Neoplasia* 2, no. 1–2 (2000): 26–40.

van Staveren, H., C. Moes, J. van Marle, S. Prahl, and M. van Gemert. Light scattering in Intralipid-10% in the wavelength range of 400–1100 nm. *Appl Opt* 30, no. 31 (1991): 4507–4514.

Wariar, R., J. N. Gaffke, R. G. Haller, and L. A. Bertocci. A modular NIRS system for clinical measurement of impaired skeletal muscle oxygenation. *J Appl Physiol* 88, no. 1 (2000): 315–325.

Zonios, G., L. T. Perelman, V. M. Backman, R. Manoharan, M. Fitzmaurice, J. Van Dam, and M. S. Feld. Diffuse reflectance spectroscopy of human adenomatous colon polyps in vivo. *Appl Opt* 38, no. 31 (1999): 6628–6637.